High-order curvilinear simulations of flows around non-Cartesian bodies.

Olivier Marsden*and Christophe Bogey†and Christophe Bailly‡
Laboratoire de Mécanique des Fluides et d'Acoustique
Ecole Centrale de Lyon & UMR CNRS 5509
69134 Ecully, France.

The current work describes the application of high-order numerical techniques to single or multiple overset curvilinear body-fitted grids, demonstrating the feasibility of direct computations of noise radiated by flows around complex non-Cartesian bodies. Flows of both physical and industrial interest can be investigated with this approach. We first rapidly describe the numerical techniques implemented in our curvilinear simulations. The explicit high-order differencing and filtering schemes are presented, as well as their application to the curvilinear Navier-Stokes equations. We then present brief results of various 2-D acoustic simulations. First the flow around a cylinder, and the associated acoustic field is described. The diameter-based Reynolds number $\mathrm{Re}_D = 150$ is under the critical Reynolds number of the onset of 3-D phenomena in the vortex-shedding. Simulation results can thus be meaningfully compared to experimental measurements. A case of acoustic scattering is then examined. A non-compact monopolar source is placed half way between two differently sized cylinders. A complex diffraction pattern is created, and resulting RMS pressure data are compared to the analytical solution. Finally the noise generated by a low Reynolds number laminar flow around a NACA 0012 airfoil is presented.

1 Introduction

The development, over the past twenty years, of high-fidelity numerical methods, has opened whole new perspectives in the domain of numerical simulations. Indeed such methods have allowed the simultaneous pursuit of two highly desirable and slightly contradictory goals, that of lowering error in terms of dispersion and dissipation, and that of reducing the necessary number of discretization points per wavelength.

It has thus become possible to simulate complex phenomena with high and quantified accuracy. This is of particular interest in the field of Computational Aeroacoustics (CAA), where several orders of magnitude separate the energy and wavelengths of propagative acoustic fluctuations from those of the flow features, and where large propagation distances are often encountered. The demands on the accuracy of the numerical schemes as well as on their capacity to cope with a small number of points per wavelength are therefore particularly stringent. Both explicit schemes, such as Tam and Webb's DRP scheme[1] or more recently those proposed by Bogey and Bailly,[2] and implicit schemes such as Lele's Padé-type,[3,4] have been shown to meet the above criteria and have been successfully applied to aeroacoustic simulations.

High-order schemes typically require large stencils, and are therefore generally implemented on structured grids. Complex curved geometries, while relatively easy to treat thanks to unstructured methods, are often impossible to mesh with a structured cartesian grid without resorting to extrapolation techniques[5] and their associated problems for the implementation of solid boundary conditions.

This difficulty can be overcome by the use of curvilinear transformations combined with overset multiple grid techniques, often referred to as Chimera techniques.[6] Such methods have sparked considerable interest over the last few years, and recent simulations have shown the feasibility of multiple grid high-fidelity simulations, in the

*Ph.D student, Olivier.Marsden@ec-lyon.fr
†CNRS research scientist, Christophe.Bogey@ec-lyon.fr
‡Professor at Ecole Centrale de Lyon, Member AIAA, Christophe.Bailly@ec-lyon.fr

fields of fluid mechanics and electromagnetics, and also more specifically in that of aeroacoustics, for example by Delfs *et al.* who used such methods to examine interactions between a vortex and an airfoil trailing edge.[7]

In this article we focus on aeroacoustic Navier-Stokes simulations, and describe our implementation of explicit high-order methods and overset grid techniques applied on curvilinear grids, as well as present results for three different configurations.

2 Curvilinear equations

High-order Large-Eddy Simulaions (LES) simulations having proven their value in the study of noise-generation mechanisms in unbounded flows, we are developing similar methods for more complex curvilinear geometries.

The full Navier-Stokes equations are solved on a computational grid which is obtained from the body-fitted grid by applying a suitable curvilinear coordinate transformation. The 2-D transformed equations can be written

$$\frac{\partial}{\partial t}\left(\frac{\mathbf{U}}{J}\right)+\frac{\partial}{\partial \xi}\left\{\frac{1}{J}\left[\xi_x(\mathbf{E_e}-\mathbf{E_v})+\xi_y(\mathbf{F_e}-\mathbf{F_v})\right]\right\}+\frac{\partial}{\partial \eta}\left\{\frac{1}{J}\left[\eta_x(\mathbf{E_e}-\mathbf{E_v})+\eta_y(\mathbf{F_e}-\mathbf{F_v})\right]\right\}=0$$

where $\mathbf{U}=(\rho,\rho u,\rho v,\rho e_t)^T$, $J=|\partial(\xi,\eta)/\partial(x,y)|$ is the Jacobian of the geometric transformation between the physical space (x,y) and the computational space (ξ,η), $\mathbf{E_e}$ and $\mathbf{F_e}$ are the inviscid fluxes and $\mathbf{E_v}$ and $\mathbf{F_v}$ the viscous ones, given by the following expressions

$$\mathbf{E_e} = \begin{pmatrix}\rho u\\ \rho u^2+p\\ \rho uv\\ (\rho e_t+p)u\end{pmatrix} \quad \mathbf{E_v} = \begin{pmatrix}0\\ \tau_{xx}\\ \tau_{xy}\\ u\tau_{xx}+v\tau_{xy}-q_x\end{pmatrix}$$

$$\mathbf{F_e} = \begin{pmatrix}\rho v\\ \rho uv\\ \rho v^2+p\\ (\rho e_t+p)v\end{pmatrix} \quad \mathbf{F_v} = \begin{pmatrix}0\\ \tau_{xy}\\ \tau_{yy}\\ u\tau_{xy}+v\tau_{yy}-q_y\end{pmatrix}$$

In the above equations, ρ refers to the fluid density, u and v to the velocity components in the x and y directions, and p to the pressure. Taking into account the perfect gas law, the total specific energy e_t is given by $e_t=p/[(\gamma-1)\rho]+(u^2+v^2)/2$. The heat term $\mathbf{q}$ is given by Fourier's law, and the components of the stress tensor $\boldsymbol{\tau}$ are those of a viscous Newtonian fluid.

3 Numerical aspects

3.1 Differencing, filtering and time integration techniques, boundary conditions

A body-fitted grid is first created around the object of interest. Grid construction is performed with care, in order to obtain grid lines of maximal regularity.

Spatial differencing in the interior part of the computational grid is performed with a high-order eleven-point explicit finite-difference formulation, optimized in the wavenumber space for perturbations of more than 4 points per wavelength, thus ensuring very low dispersion and dissipation. Information on the properties of the differencing formulations as well as on the optimization parameters can be found in Bogey & Bailly.[2] The partial derivatives of the transformation's Jacobian matrix are also calculated with the above scheme, using the expression

$$J_{i,j}=\frac{(-1)^{i+j}J^{-1}_{j,i}}{|J^{-1}|}$$

for a 2-D transformation. Care must be taken to ensure that metric identities imposing the commutative properties of partial differentials are respected.[8,9] Close to solid boundaries, differencing is performed with lower order stencils, first with the traditional centered 7-point DRP[1] stencil and then with centered and finally non-centered 5-point fouth order stencils. A no-slip solid-wall boundary condition is applied by imposing $u=v=0$ at the boundary, and also $\partial p/\partial n=0$ thanks to a one-sided 5-point stencil.

Time integration is performed with an explicit 6-stage Runge-Kutta algorithm developed by Bogey *et al.*[2] It is optimized in the wavenumber space, to minimize both dispersion and dissipation for angular frequencies up to $\omega\Delta t = \pi/2$, and is implemented in low-storage form. Stability is guaranteed up to angular frequencies verifying $\omega\Delta t = 1.25 \times \pi$.

The very low dissipation exhibited by the numerical algorithm means that high-frequency numerical instabilities of various origins are not naturally damped over time. In this work, these unwanted oscillations are eliminated with a low-pass filter. The main desired property for the filter is high selectivity. To this end, an eleven-point explicit optimized filter[2] is used on the interior of the transformed domain every few time steps. The frequency of the filtering depends on the smoothness or quality of the computational grid, and varies in the simulations presented here from every time step for the airfoil to every five time steps for the cylinder flow. The relative dissipation of the filter is inferior to 5×10^{-3} up to four points per wavelength, and rapidly increases to one for grid-to-grid oscillations. This very high selectivity allows the use of a small filtering coefficient, typically inferior to 0.1 inside the computational domain.

Close to boundaries, the centered high-order filters described above cannot be used. Unfortunately, boundary conditions tend to generate spurious high-frequency oscillations, rendering some form of filtering necessary. Previously, lower order centered filters were used, inducing higher dissipation and dispersion close to solid boundaries. To alleviate this problem, non-centered 11-point highly selective filters were designed by Berland *et al.*[10] which make it possible to maintain filtering quality at boundaries. More information on these filters, as well as the individual coefficients, can be found in ref.[10]

3.2 Overset grid techniques

The use of curvilinear body-fitted grids is often not sufficient to allow high-fidelity simulations around complex objects. The development of multiple overset curvilinear grid techniques is therefore of great interest regarding the generalization of complex aeroacoustic simulations, especially when multiple bodies are involved. With this approach, each object or in some cases part of an object, is first surrounded by a structured body-fitted grid. The grids either overlap each other sufficiently to ensure that the whole physical domain is covered, or are embedded in an underlying cartesian grid that spans the entire area of interest. During the simulation, the boundary points in the overlapping zones are updated by interpolating their values from those of the donor grid.

The quality of the interpolation depends essentially on the precise knowledge of the receiving point coordinates with respect to the donor grid, and on the chosen interpolation method. Generally, donor and receiver points are not coincident, so the receiver point coordinates with respect to the donor grid are not known *per se*. They must be calculated with care, especially when high-order interpolation is subsequently used. The interpolation method adopted here is described for a 2-D application, but can be generalized to three dimensions. Indeed, the interpolated value at a receiving point P is obtained thanks to $N+1$ successive interpolations in perpendicular directions on the donor grid, as shown on Figure 1 for a 2-D case. N is the stencil size of the interpolation.

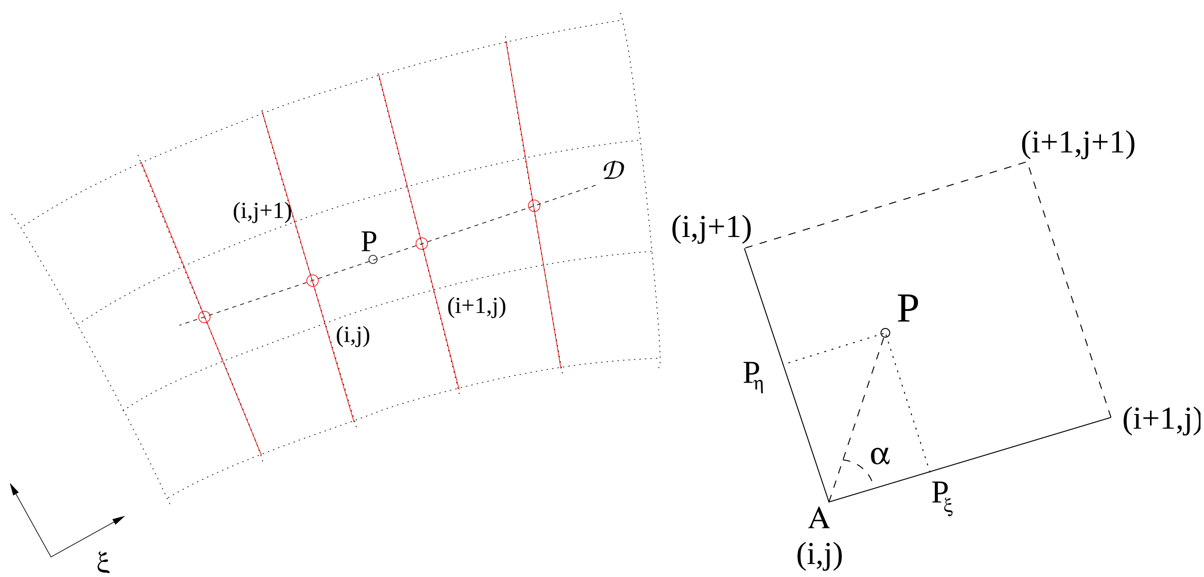

Figure 1: **2-D interpolation method**. Coordinates P_ξ and P_η of the receiving point P with respect to the underlying donor grid are used to perform successive 1-D interpolations parallel to ξ and η grid lines.

First, interpolation is carried out in the η direction with the P_η coordinate, to calculate the values at the N intersection points of the line $\mathcal{D}$ with the η grid lines. The value at the point P is then interpolated from the N values previously calculated, with the P_ξ coordinate. In order to speed up the overall interpolation process, coordinates of the receiver point projected on the donor grid, as well as those of the N intersection points are calculated at the end of the grid generation phase and stored for quick retrieval during the simulation. Nevertheless, the current implementation of high-order Lagrangian interpolation remains computationally expensive and slow.

Different single-dimension interpolation techniques have been examined, and in particular cubic splines and Lagrange polynomial functions of varying orders. Figures 2 show a comparison beetween four interpolating functions: Lagrange polynomials on eleven and seven points, and spline functions on six and four points. The local error function for the wavenumber $\alpha = 2\pi/\lambda$ corresponding to the wavelength λ is defined by

$$E^{1/2}(\alpha) = \left(\int_0^\lambda \left(\hat{f}_\alpha(\delta x) - f_\alpha(\delta x) \right)^2 \delta x \right)^{\frac{1}{2}}$$

where $\hat{f}_\alpha(x)$ represents the interpolated value of f_α at point x, and $f_\alpha(x) = \sin(\alpha x)$. While the interpolation error certainly diminshes with the interpolation order, it is interesting to note that the six-point spline outperforms the seven-point Lagrange polynomial for wavenumbers verifying $\alpha\Delta x > 0.85$, that's to say for waves discretized by less than 7.4 points per wavelength.

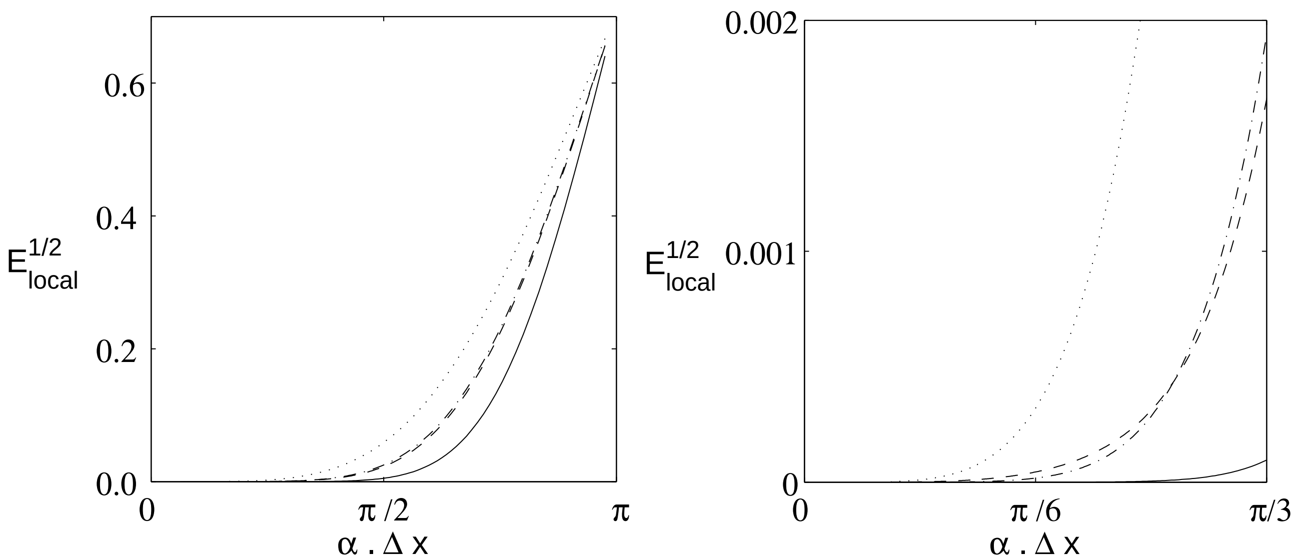

Figure 2: **Interpolation function comparison.** ········ four-point spline, –·–·– six-point spline, – – – seven-point Lagrange polynomials, ——— eleven-point Lagrange polynomials.

The precision required of the interpolation depends on the simulation being carried out. For example in acoustic scattering simulations such as the two-cylinder diffraction problem described later in this work, errors generated at the grid interfaces by the interpolation process are simply propagated away and therefore result in roughly of the same order of error on the calculated pressure field. On the other hand, in cases where inhomogenous flow crosses the interpolation interface, relatively small interpolation errors can lead to unacceptably large modifications in the radiated pressure field.

4 Test cases

4.1 Cylinder at a Reynolds number of 150

The first test case is that of the flow around a cylinder. As the current simulation code is 2-D, a very low Reynolds number $\mathrm{Re}_D = U_\infty D/\nu$ of 150, where D is the cylinder diameter, was chosen in order to remain below the onset of three-dimensional behaviour in the wake, which seems to appear[11] between Reynolds numbers of 160 to 180. This should enable a reasonable comparison between experimental flow results and the present numerical simulation.

The upstream Mach number of the flow around the cylinder is $M_\infty = 0.33$, and the cylinder diameter $D = 2 \times 10^{-5}$ m. The radial step at the cylinder wall is $D \times 0.01$, and the grid dimensions are 500 points in the radial direction by 300 points in the azimuthal direction. An ten-point overlap in the wake region is used to impose a periodic condition in the azimuthal direction. The five points of overlap at each azimuthal extremity of the computational grid thus allow the use of the eleven-point differencing and filtering scheme around the entire grid circumference.

Various flow characteristics are compared to those given by previous numerical and experimental studies of low Reynolds number cylinder flows.
The Strouhal number, which characterizes the frequency the von Kármán vortex street behind the cylinder, is found to be 0.184, in perfect agreement with other values as is shown on Figure 3.

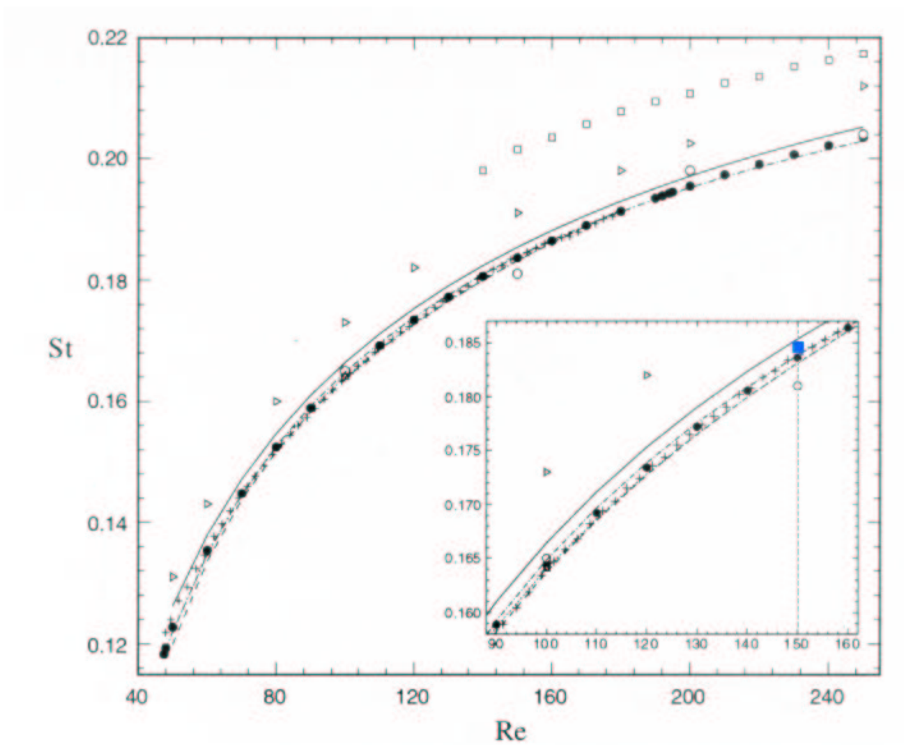

Figure 3: **Comparison of our calculated Strouhal number with various experimental and numerical studies**, extracted from Posdziech and Grundmann.[12] ■ : present simulation.

The mean drag coefficient C_D of 1.32, illustrated on Figure 4, shows good agreement with both experimental data[13,11] and recent numerical studies.[14,15,12] Likewise, the RMS lift coefficient C_L' of 0.37 compares favorably with numerical simulations performed by both Zhang and Kravchenko.

Finally, velocity profiles in the cylinder wake compare perfectly over a large downstream distance to those given by an autosimilar analytical solution for a plane wake, as illustrated on Figure 4.1. The physics of the cylinder flow thus appear to be correctly captured by the present simulation.

Thanks to the high precision and low dissipation of the numerical scheme, the radiated pressure waves are preserved over the entire computational domain, as it can be seen in the Figure 5. The acoustic radiation is almost perfectly dipolar, with negligeable a quadrupolar contribution, as expected for a low-Mach number cylinder flow.[16] Our radiation levels have not been verified, for lack of experimental acoustic results at such a low Reynolds number, and because of the difficulty in reproducing a properly 2-D configuration.

The theory of vortex sound applied to the æolian tone problem by Crighton[17] and Howe[18] shows that the dipolar acoustic radiation is created by the diffraction of quadrupolar aerodynamic sources in the near cylinder wake. With this view in mind, Figures 6 , 7 and 8 represent the evolution over one period T_p of the near-cylinder vorticity field, pressure field and a source term proposed by Powell[19] and defined by

$$S = \rho_\infty \nabla . (\boldsymbol{\omega}' \times \mathbf{v}')$$

where $\boldsymbol{\omega}' = \boldsymbol{\omega} - \overline{\boldsymbol{\omega}}$ is the fluctuating vorticity and $\mathbf{v}' = \mathbf{v} - \overline{\mathbf{v}}$ is the fluctuating speed. It should be noted that only the non-linear part of the original formulation is considered here. A distribution of quadrupolar nature can be seen in the cylinder wake, centered roughly one cylinder diameter downstream from the cylinder edge. The intensity of S farther downstream in the cylinder wake diminishes rapidly.

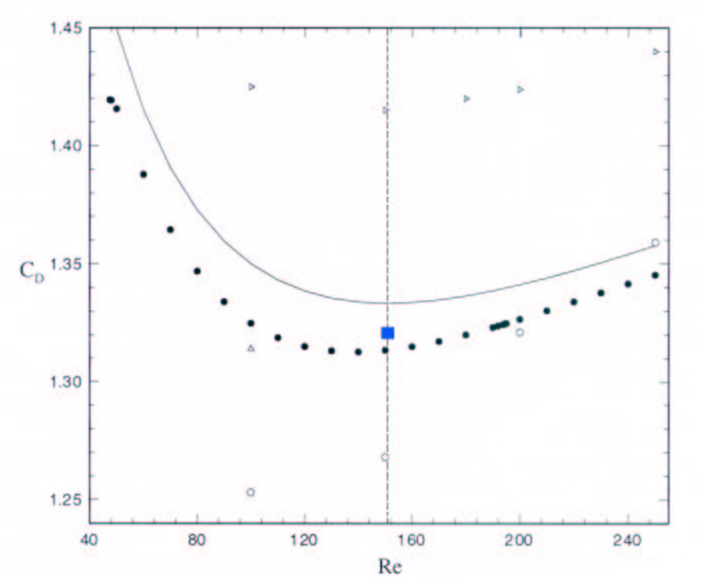

Figure 4: **Evolution of the drag coefficient with the Reynolds number .**
—: Henderson (1995), ▷: Zhang *et al* (1995), □: Thompson *et al* (1996), ○: Persillon et Braza (1998), △: Kravchenko *et al* (1999), •: Posdziech et Grundmann (2001), ■ current work

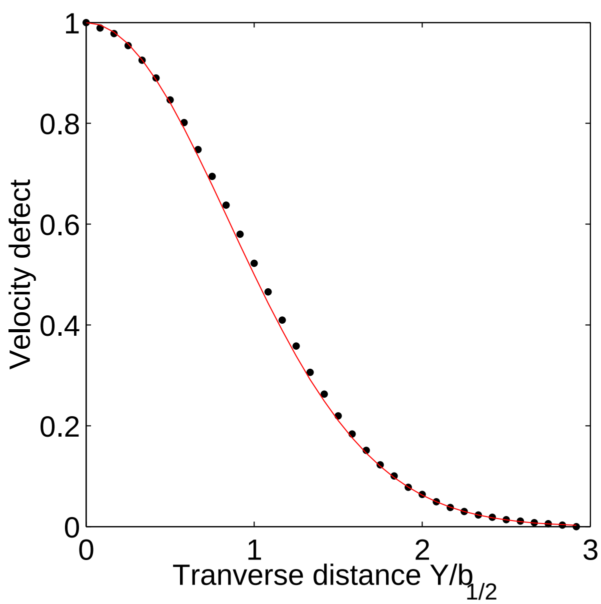

Mean velocity profile in the cylinder wake region

Velocity deficit vs. transversal distance. – 2-D analytical autosimilar solution
• Simulated values

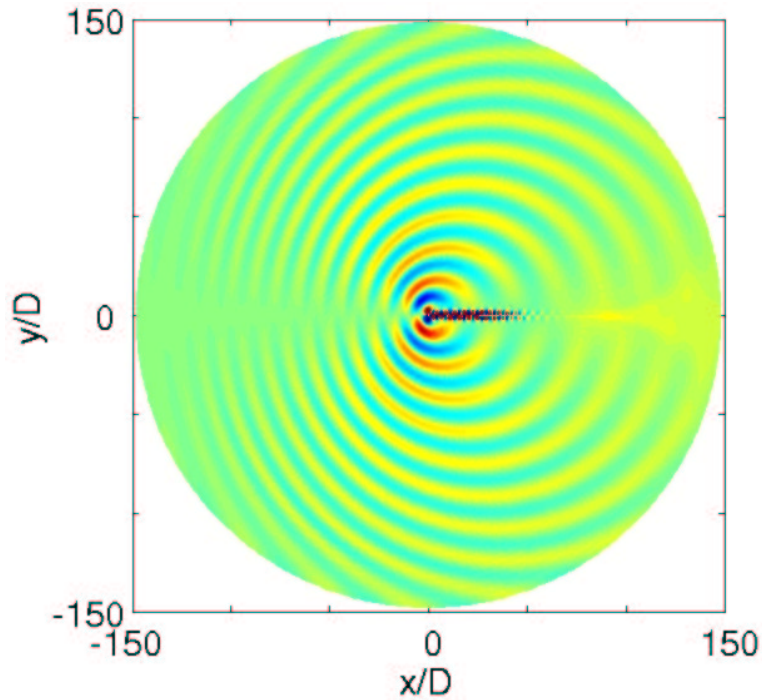

Figure 5: **Instantaneous pressure field around a cylinder at a Reynolds number of 150 and Mach number of $\mathbf{M_\infty = 0.33}$** Distance is rendered non-dimensional by the cylinder diameter D. Pressure colour scale is between -200 and 200 Pa.

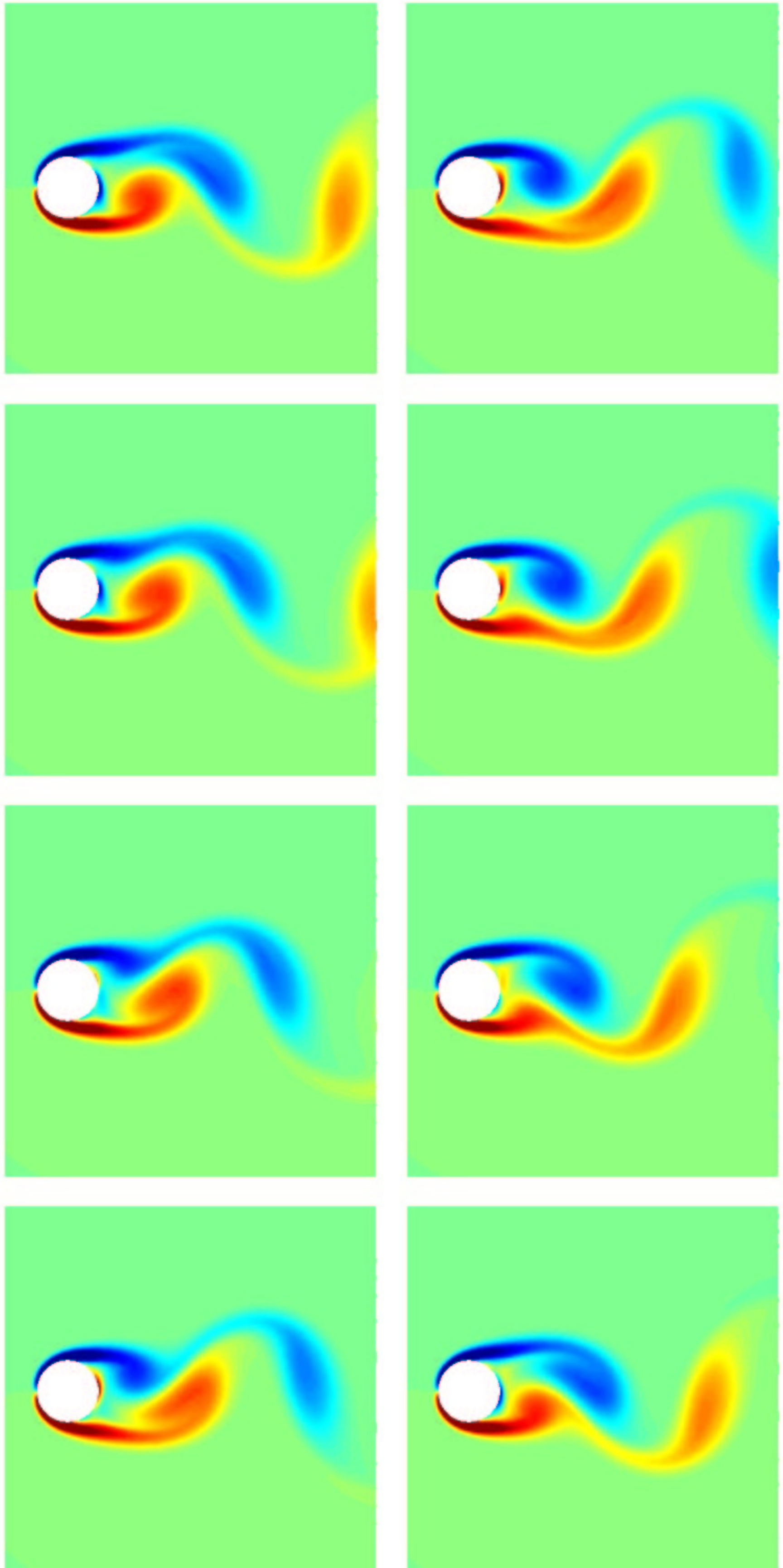

Figure 6: **Vorticity around the cylinder plotted over one period of the vortex shedding.** Colour scale is between -3×10^7 and 3×10^7, and the domain shown spans $-D$ to $5D$ in the x direction and $-3D$ to $3D$ in the y direction. The time-step between two snapshots is $T_p/9$.

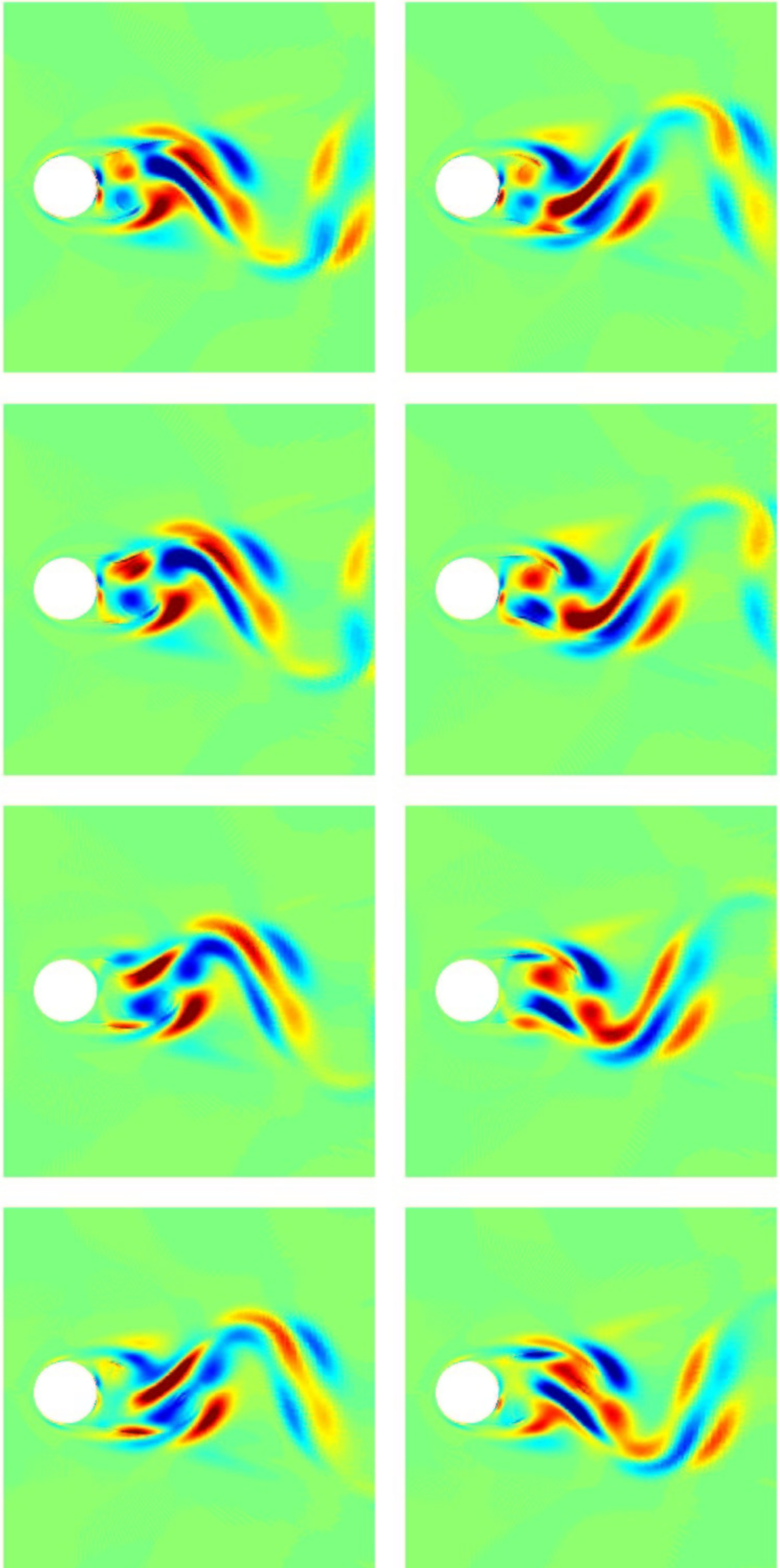

Figure 7: **Source term $S = \nabla.(\rho\boldsymbol{\omega}' \times \mathbf{v}')$.** Its opposite is plotted over one period of the vortex shedding. Domain shown spans $-D$ to $5D$ in the x direction and $-3D$ to $3D$ in the y direction. The time-step between two snapshots is $T_p/9$.

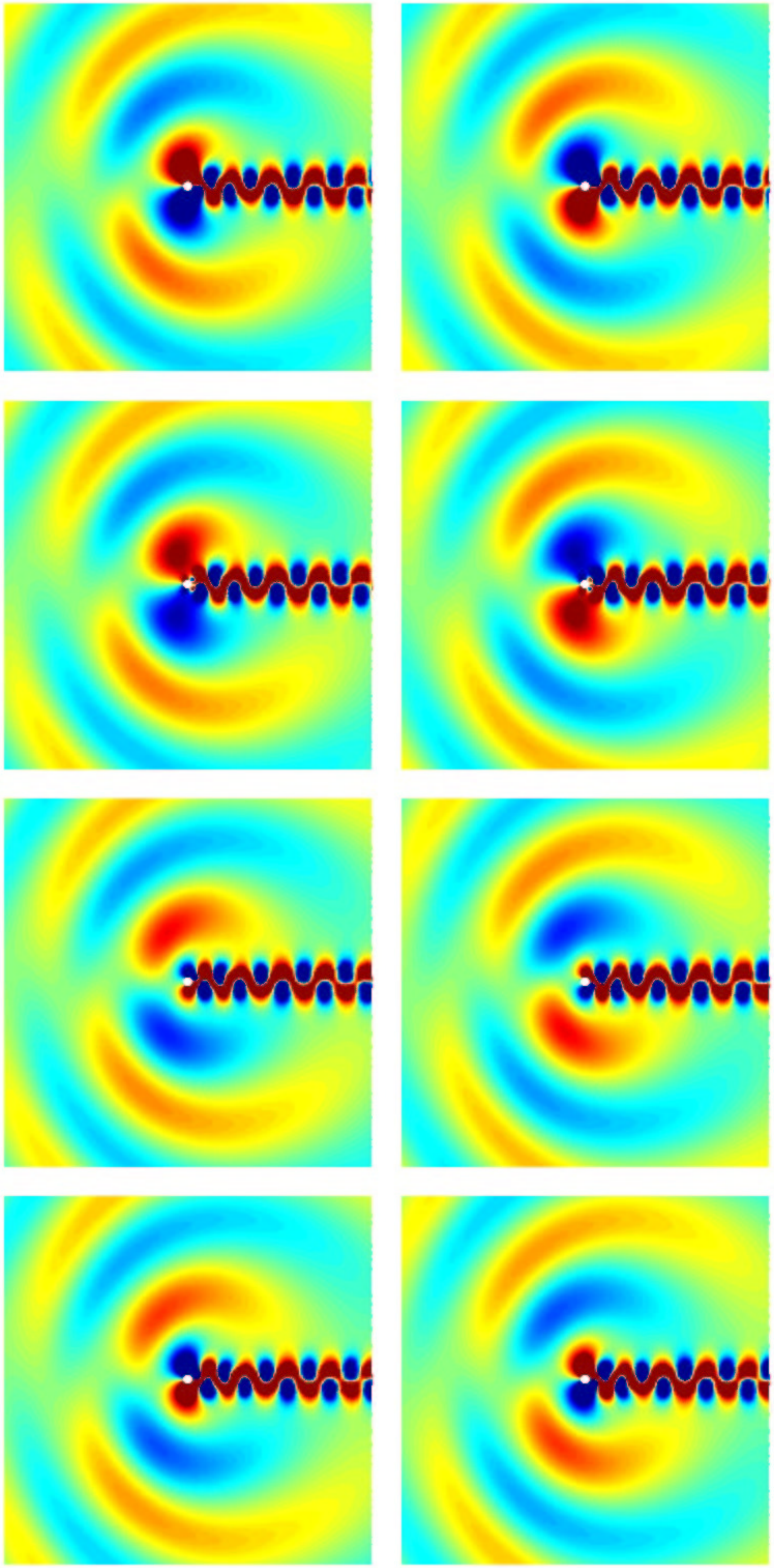

Figure 8: **Fluctuating pressure around the cylinder plotted over one period of the vortex shedding.** Colour scale is between -1000 and 1000 Pa, and the domain shown spans $-20D$ to $20D$ in both x and y directions. The time-step between two snapshots is $T_p/9$.

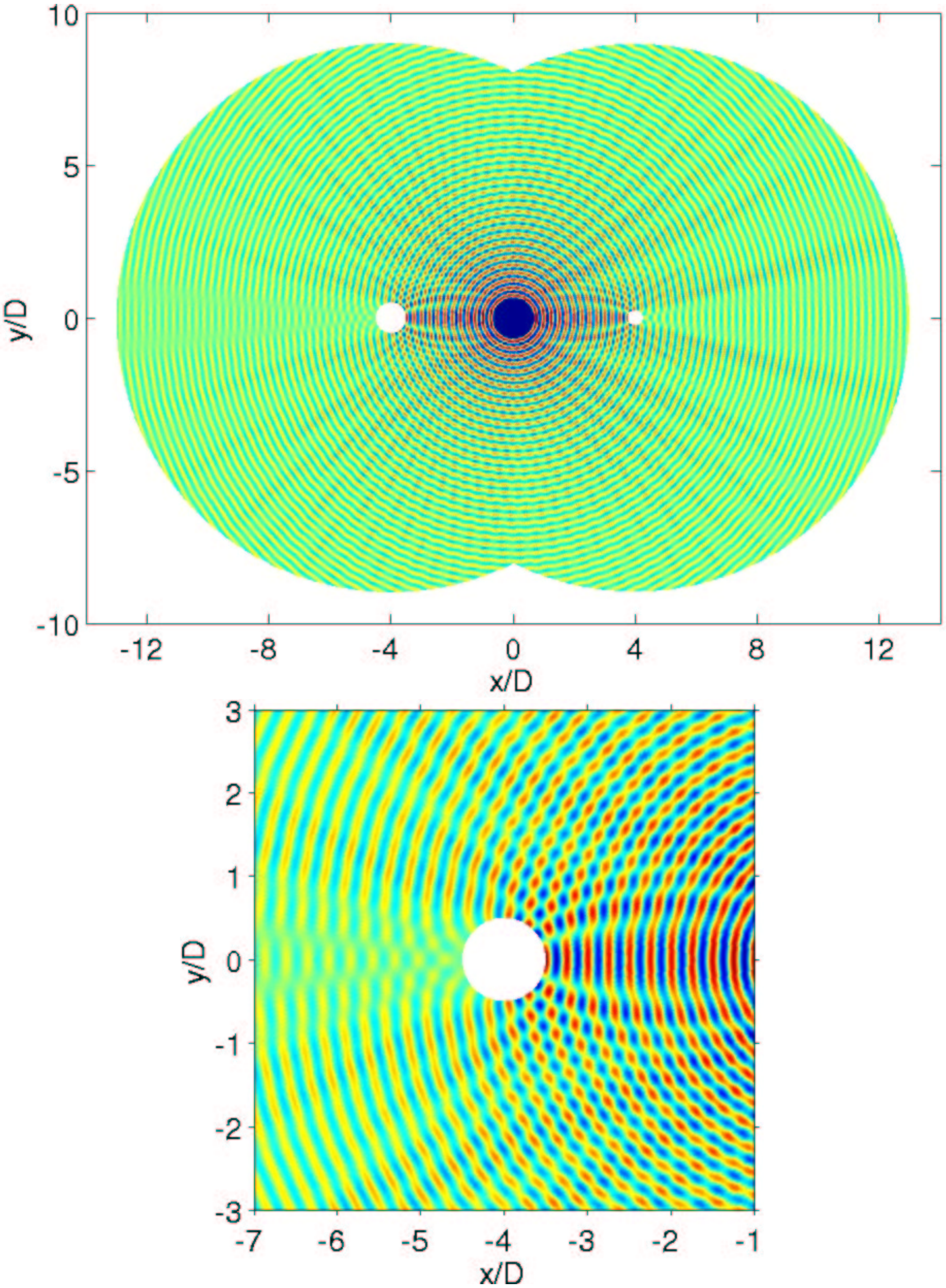

Figure 9: **Two cylinder diffraction problem**. Snapshot of the fluctuating pressure field over the entire computational domain, and a closer view of the pressure field around the larger left cylinder. Pressure colour scale is between -10^{-6} and 10^{-6} Pa.

4.2 Diffraction by two cylinders

The second test-case presented here is the diffraction of sound by two circular cylinders of different diameters, as presented in the proceedings of the 4^{th} CAA workshop.[20] All distances are rendered non-dimensional by the larger cylinder's diameter D. The smaller cylinder's diameter is half that of the larger, and the separation between the two cylinders is $8D$. The sound source is a non-compact monopole located half way between the two cylinders, whose expression is given by

$$S = \sin(\omega t)\,\exp\left(-\ln 2\,\frac{x^2+y^2}{b^2}\right)$$

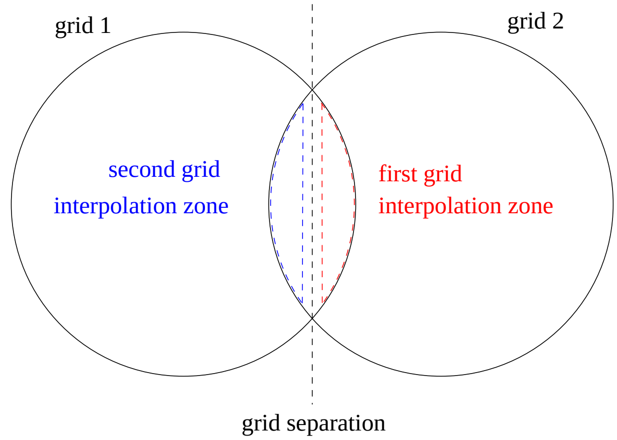

Figure 10: **Grid construction for two-cylinder diffraction**. A circular grid is built around each cylinder, and the resulting overlap zone is used to allow communication between the two grids.

where $b = 0.2$ is the gaussian half-width of the source and $\omega = 8\pi$ its angular frequency with a time-scale of D/c_∞. A highly complex pressure diffraction pattern is generated by this configuration, providing a challenging test for the curvilinear solver. It should be noted that the test-case difficulty is greatly dependent on the type of simulation. Indeed, to obtain errors of less than one percent of maximum diffracted RMS fluctuations, a linearized Euler solver need only ensure a dynamic range of around 1×10^{-7}, *i.e.* one hundredth of the RMS fluctuations amplitude, whereas a non-linearized solver must achieve a dynamic range that is five orders of magnitude higher. This test-case is therefore a severe challenge for our non-linearized solver.

Figure 9 shows a snapshot of the instantaneous pressure field around the two cylinders.

The overset grid approach presented above was used to perform the simulation. A circular grid was built around each cylinder, with a central zone where both grids overlap, as shown on Figure 10. Grid sizes were 700 points in the azimuthal direction by respectively 360 and 400 points in the radial direction for the larger and smaller cylinder. This corresponded to a spatial discretization of eight points per wavelength on average, with tighter spacing close to the cylinders. The interpolation zones thus created contained roughly 5700 points for each grid. Simulation time was of the order of 2.5 hours per 1000 iterations on a 2GHz Intel Xeon processor, one period of the monopolar source requiring 140 iterations. The RMS results presented underneath were calculated over 5 periods, after an initial 140 periods of simulation, corresponding roughly to 20000 iterations.

The different interpolation functions mentioned above were examined. Four-point spline interpolation yielded poor results, resulting in overly low and slightly displaced RMS pressure maxima. Six-point splines and seven-point Lagrange polynomials both showed very similar results, considerably better than those obtained with four-point spline interpolation. However, errors of slightly less than 5% remain on the calculated RMS pressure field. The RMS pressure values along the horizontal $y = 0$ axis are plotted on Figure 11.

Additional simulations were subsequently performed with eleven-point Lagrange polynomials, to ascertain the origin of the remaining errors. A simulation with interpolation based on eleven-point Lagrange polynomials was undertaken on an identical grid, and yielded identical results, indicating that the residual errors in the spline simulation were not due to the choice of spline interpolation. Another simulation with the same spline interpolation and with smaller mesh sizes yielded improved results. Having checked that this improvement was not linked to the inside numerical scheme, it was deduced that the calculation of the interpolation point coordinates with respect to the donor grid was majoritarily responsible for the remaining discrepancies in the calculated RMS data. The current coordinate calculation relies on bilinear interpolation, so in the future we will examine the benefits of using bicubic interpolation, which should already substantially reduce coordinate calculation imprecisions.

4.3 Noise generated by an airfoil in a laminar flow

Finally we show an example of the calculation of the noise radiated by a NACA 0012 airfoil in a laminar flow. The airfoil chord c measures 8 mm and the radial step at the boundary wall is 5×10^{-4}c.

The computational grid has 1000 points in the azimuthal direction and 200 in the radial direction, and is of C-type,[21] with an overlap in the wake zone. Careful attention was payed to grid construction to minimize oscillations in the Jacobian matrix coefficients. Indeed it is well known that high-order difference schemes inevitably generate oscillations when they are applied to sudden discontinuities.[22,9] The trailing edge is a particularly sensitive grid zone since such discontinuities for terms such as $\partial\xi/\partial x$ cannot be avoided with resorting to a relatively costly interpolation technique. To minimize problems in the vicinity of the trailing

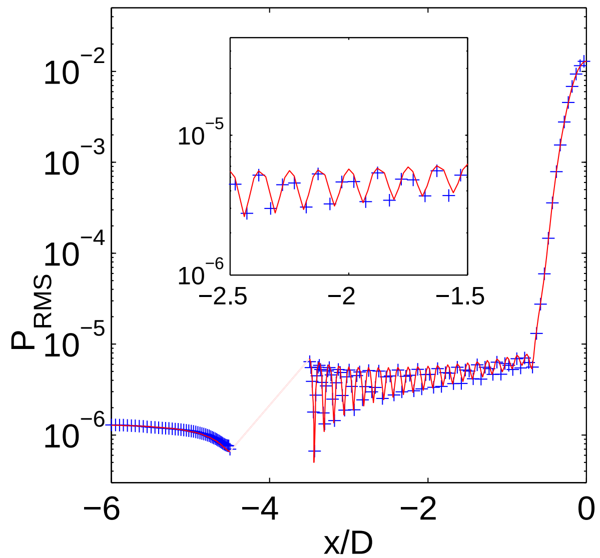

Figure 11: **RMS pressure on the horizontal axis between the two cylinders**. — analytical solution by Visbal and Sherer (to appear in J. Acoust. Soc. Am.), + simulated values.

edge, radial (η) grid lines are not perpendicular to the airfoil boundary, which allows us to impose a continuous variation for three of the four terms in the Jacobian matrix. Only $\partial\eta/\partial x$ remains necessarily problematic. Grid smoothing is performed, to reduce differences in size between upstream meshes, which are large because of the very small radius of curvature at the airfoil leading edge, and the considerably smaller downstream meshes. Moreover, during the simulation explicit high-order filtering with a larger coefficient than over the rest of the computational domain removes the spurious high-frequency oscillations generated by the discontinuous fourth Jacobian term. Figure 12 shows the central portion of the final grid around the airfoil.

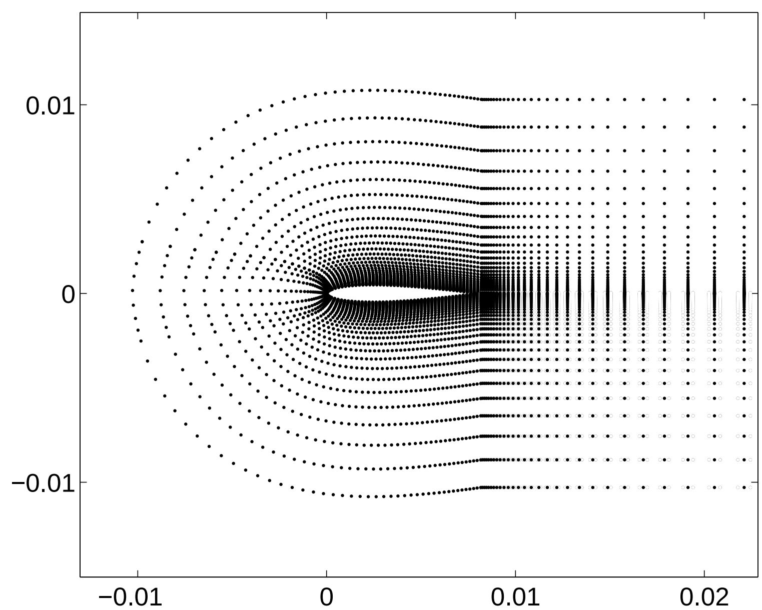

Figure 12: **Central grid around a NACA 0012 airfoil.**

So far we have limited our simulations to relatively low Reynolds numbers. The chord-based Reynolds number of the simulation presented here is around $\mathrm{Re}_c = 60000$, at a Mach number of $\mathrm{M}_\infty = 0.33$. This low Reynolds number generates a steady and regular flow structure around the airfoil, with a von Kármán-like vortex-street in the wake zone. As expected, the resulting acoustic radiation is strongly dipolar, with a marked upstream directivity. Figure 13 presents a snapshot of the instantaneous fluctuating pressure field around the airfoil.

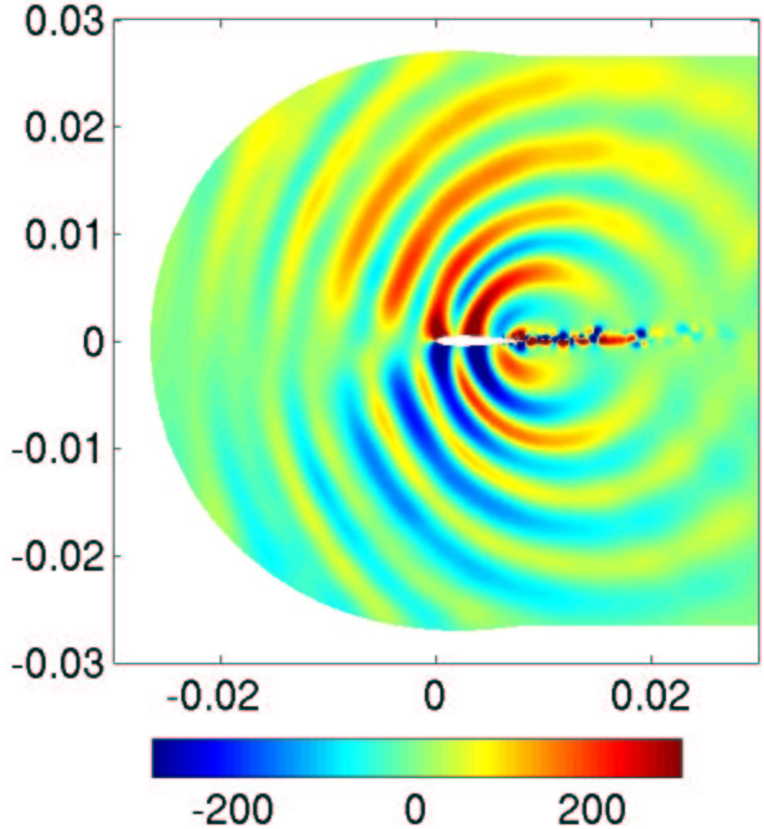

Figure 13: **Fluctuating pressure field around a NACA 0012 airfoil at $\mathrm{Re}_c = 60000$ and $M_\infty = 0.33$** Pressure colour scale is between -300 and 300 Pa.

5 Conclusions and future developments

A high-fidelity curvilinear solver with multiple overset grid capability has been shown to give good results for various 2-D aeroacoustic simulations, both with and without flow. The simulated flow around a cylinder at a very low Reynolds number is in very good agreement with experimental and numerical studies, and acoustic radiation is preserved over the entire computational domain. Acoustic scattering by a two-cylinder layout compares favorably with analytical results. Finally a low Reynolds number flow around an airfoil is presented.

Numerical resolution is performed with eleven-point explicit optimized finite-difference schemes and low-pass filters, combined with an explicit six-step low-storage optimized Runge-Kutta algorithm. Non-centered high-order filters are used near computational boundaries. Different interpolation methods have been implemented and tested for the overset grid communication process, with six-point spline showing promising results. The acoustic scattering simulation showed the importance of accurately calculating the coordinates of receiving grid points with respect to the donor grid. To this end, bicubic interpolation will be tested for the coordinate point calculation.

Our main goal now is to complete the development of the 3-D solver to allow the realistic simulation of complex high Reynolds number flows. It will maintain the general structure of the current code based on the resolution of the curvilinear Navier-Stokes equations with high-order explicit spatial and temporal schemes, and will rely on overset grid techniques to be able to examine multiple bodies of complex geometries.

Acknowledgements

This work was undertaken with the financial support of Electricité de France, Direction Recherche & Développement under the supervision of Dr. Philippe Lafon.

References

[1]C.K.W. Tam and J.C. Webb. Dispersion-relation-preserving finite difference schemes for computational acoustics. *J. Comput. Phys.*, 107:262–281, 1993.

[2]C. Bogey and C. Bailly. A family of low dispersive and low dissipative explicit schemes for noise computations. *J. Comput. Phys.*, 194(1):194–214, 2004.

[3]S.K. Lele. Compact finite difference schemes with spectral-like resolution. *J. Comput. Phys.*, 103:16–42, 1992.

[4]M. Visbal and D. Gaitonde. High-order-accurate methods for complex unsteady subsonic flows. *AIAA Journal*, 37(10):1231–1239, 1999.

[5]K.A. Kurbatskii and C.K.W. Tam. Cartesian boundary treatment of curved walls for high-order computational aeroacoustics schemes. *AIAA Journal*, 35(1):133–140, 1997.

[6]J.A Benek, J.L. Steger, F.C. Dougherty, and P.G. Buning. Chimera: A Grid-Embedding Technique. *AEDC-TR-85-64*, 1986.

[7]M. Lummer, J. W. Delfs, and T. Lauke. Simulation of sound generation by vortices passing the trailing edge of airfoils. *AIAA Paper 2002-2578*, 2002.

[8]P.D. Thomas and C.K. Lombard. The Geometric conservation law - a link between finite-difference and finite-volume methods of flow computation on moving grids. *AIAA Journal*, 17(10):1030–1037, 1978.

[9]M. Visbal and D. Gaitonde. On the use of higher-order finite-difference schemes on curvilinear and deforming meshes. *J. Comput. Phys.*, 181:155–185, 2002.

[10]J. Berland and C. Bogey, C.and Bailly. Optimized explicit schemes: Matching and boundary schemes, and 4th-order runge-kutta algorithm. *AIAA Paper 2004-2814*, 2004.

[11]H. Zhang, U. Fey, B.R. Noack, M. Knig, and H. Eckelmann. On the transition of the cylinder wake. *Phys. Fluids*, 7(4):779–794, 1995.

[12]O. Posdziech and R. Grundmann. Numerical simulation of the flow around an infinitely long circular cylinder in the transition regime. *Theoret. Comput. Fluid Dynamics*, 15(2):121–141, 2001.

[13]C.H.K Williamson. Oblique and parallel modes of vortex shedding in the wake of a circular cylinder at low Reynolds numbers. *J. Fluid Mech.*, 206:579–627, 1989.

[14]A. Persillon and M. Braza. Physical analysis of the transition to turbulence in the wake of a circular cylinder by three-dimensional Navier-Stokes simulation. *J. Fluid Mech.*, 365:23–88, 1998.

[15]A.G. Kravchenko, P. Moin, and K. Shariff. B-spline method and zonal grids for simulations of complex turbulent flows. *J. Comput. Phys.*, 151:757–789, 1999.

[16]F. Pérot, J.M. Auger, H. Giardi, X. Gloerfelt, and C. Bailly. Numerical prediction of the noise radiated by a cylinder. *AIAA Paper 2003-3240*, 2003.

[17]D.G. Crighton. Basic principles of aerodynamic sound generation. *Prog. Aerospace Sci.*, 16(1):31–96, 1975.

[18]M.S. Howe. *Acoustics of fluid-structures interactions.* Cambridge University Press, 1998.

[19]A. Powell. Theory of vortex sound. *J. Acoust. Soc. Am.*, 36:177–195, 1964.

[20]S. Sherer and M. Visbal. Computational study of acoustic scattering from multiple bodies using a high-order overset grid approach. *AIAA Paper 2003-3203*, 2003.

[21]J. F. Thomson, B.K. Soni, and N.P. Weatherill. *Handbook of Grid Generation.* CRC Press, 1999.

[22]R. Vichnevetsky. Propagation through numerical mesh refinement for hyperbolic equations. *Math. Comp. Simulation*, XXIII, 1981.